PNAS
www.pnas.org

Supplementary Information for

# Multiple domain interfaces mediate SARM1 autoinhibition.

Chen Shen[a,b,1], Mihir Vohra[c,1], Pengfei Zhang[a,b], Xianrong Mao[c], Matthew D. Figley[e], Jian Zhu[c], Yo Sasaki[c], Hao Wu[a,b,*], Aaron DiAntonio[d,e,*], and Jeffrey Milbrandt[c,d,*]

[a]Department of Biological Chemistry and Molecular Pharmacology, Harvard Medical School, Boston, MA 02115; [b]Program in Cellular and Molecular Medicine, Boston Children's Hospital, Boston, MA 02115; [c]Department of Genetics, Washington University School of Medicine, St. Louis, MO 63110; [d]Needleman Center for Neurometabolism and Axonal Therapeutics, Washington University School of Medicine, St. Louis, MO 63110; [e]Department of Developmental Biology, Washington University School of Medicine, St. Louis, MO 63110;
[1]C.S. and M.V. contributed equally to this work.

*Correspondence to: wu@crystal.harvard.edu, diantonio@wustl.edu, jmilbrandt@wustl.edu

**This PDF file includes:**

## Materials and Methods

**Peptide Design and Synthesis.** Peptides were designed to be roughly 24 amino acids long with the goal of keeping evolutionarily conserved regions intact. Peptides were synthesized by GenScript to >80% purity.

**Protein Expression and Purification.** SARM1 proteins used for HPLC were expressed and purified from HEK293T cells as previously described (1). When expressing constitutively active SARM1 mutants, we used NRK1-HEK293T cells, a line stably expressing nicotinamide riboside kinase 1 (NRK1) so that addition of nicotinamide riboside (NR) would increase cellular $NAD^+$ levels despite SARM1 activity, promoting cell viability until harvesting. 24 h after plating, cells were transfected with SARM1 containing an N-terminal StrepTag (and treated with 1 mM NR if appropriate). 48 h later, cells were collected and lysed and purification was performed using MagStrep (Strep-Tactin) type 3 XT beads (IBA Lifesciences). Purified protein on MagStrep beads was stored at -80°C.

For cryo-EM study of the SARM1 octamer, the human SARM1 sequence (20-700) was cloned into the pDEST-636 vector to generate a construct with N-terminal TEV-cleavable MBP-tag. The construct was transformed into *E. coli* DH10Bac cells to produce the baculovirus. MBP-tagged SARM1 was expressed by infecting SF9 cells with the P3 generation virus. After 48 h expression at 300 K, cells were harvested and sonicated in a lysis buffer containing 20 mM Tris at pH 7.4, 150 mM NaCl, 1mM TCEP (Buffer A), supplemented with one tablet of protease inhibitor cocktail (Sigma: S8820). After ultracentrifugation at 42,000 rpm for 1 h, the supernatant was collected and incubated with amylose resin for 1 h. The resin was washed with Buffer A, and the target protein was eluted with Buffer A supplemented with 25 mM maltose. The eluate was then injected into a Superdex 200 gel filtration column in Buffer A. Fractions containing MBP-SARM1 were collected for further cryo-EM study.

**Electron Microscopy (EM) Data Collection.** Purified MBP-SARM1 at 1.6 mg/ml (3 µl) was applied to glow-discharged Quantifoil grids (R 1.2/1.3 400 mesh, copper, Electron Microscopy Sciences), blotted for 4 s in 100% humidity at 4 °C, and plunged into liquid ethane using an FEI Vitrobot Mark IV. The grids were imaged using an FEI Titan Krios microscope operating at 300 keV (Harvard Medical School Cryo-EM Core Facility) equipped with a K3 direct electron detection camera, and 4,776 movies were collected in a counting mode at 0.825 Å physical pixel size with 60 total frames and 69.2 e/per $Å^2$ accumulated dose per movie.

**Cryo-EM Image Processing and Model Refinement.** A complete follow chart of image processing and model refinement is shown in Fig. S4. Collected movie frames were motion-corrected and dose-weighted by MotionCor2 (2). Initial contrast transfer function (CTF) parameters were estimated by CTFFIND4 (3), and particle picking was carried out using crYOLO (4). In total, 900,703 particles were selected, binned to pixel size 2.346 Å and subjected to reference-free 2D classification in Relion (5). Following successive 2 rounds of 2D and 3D classifications using an initial model generated in Relion, we reconstructed a 3D-refined map (Model X) from 14,831 particles using C8 symmetry. Using Model X as an initial model, we selected particles from round 1 2D classification to perform 3D classification, followed by 3D refinement on a selected class using C8 symmetry. After per particle CTF refinement, Bayesian polishing and postprocessing in Relion, the final volume reached a resolution of 3.4 Å, as measured by gold standard Fourier shell correlation (FSC) between half maps. To further improve the resolution at the TIR domain, Relion-based symmetry expansion was carried out, and density subtraction was performed to leave just the TIR domain region intact. The subtracted particle set was subjected to 3D classification without alignment. The class with the most homogeneous particles was selected, reverted to original, unsubtracted particles, and refined to an overall resolution of 3.7 Å. This TIR-focused map exhibited significant improvement of TIR domain density in a local resolution assessment by ResMap (6).

For model building, ARM1 region (1-307) and ARM2 region (308-398) sequences were submitted to SWISS-MODEL (7) to generate two independent models, which were fitted as rigid

bodies into the TIR-focused cryo-EM map. The initial models of SAM and TIR domains were from the crystal structures with PDB ID-6O0S and 6O0Q, respectively (8). All manual adjustments were done in Coot (9), and PHENIX (10) was used to refine the models against cryo-EM density maps. All representations of electron densities and structural models were generated using ChimeraX (http://www.rbvi.ucsf.edu/chimerax/) and Pymol (11).

**In vitro NADase Assay and Metabolite Extraction.** Purified protein on beads was incubated with peptides for 30 min at 37°C. We then added 2.5 μM $NAD^+$ (Sigma) to a total volume of 20 μl and let the reaction proceed for 2 h at 37°C. For each purified SARM1 construct, we used sufficient SARM1 attached to beads to consume roughly half the added $NAD^+$ in the absence of peptide. Metabolites were extracted with the chloroform/methanol method, lyophilized, and stored at -20°C as previously described (1) until measurement by HPLC.

**High Performance Liquid Chromatography.** Lyophilized samples were resuspended in 10 μl 0.5M potassium phosphate buffer and metabolites were analyzed by HPLC (Nexera X2) with a Kinetex (100 x 3 mm, 2.6 μm; Phenomenex) column. Internal standards for $NAD^+$, nicotinamide, and ADPR were used to identify the respective products and generate standard curves. For each sample, SARM1 activity was calculated as the area under the ADPR curve divided by the area under the ADPR curve of the control sample which had SARM1, $NAD^+$, and no peptide.

**Lentivirus Production**. Lentiviral particles were made from HEK293T cells as previously described (12). Plasmids containing SARM1 constructs followed by a self-cleaving 2A peptide and Venus were co-transfected with viral packaging proteins and VSVG. 48 h later, lentiviral particles in the media were collected and concentrated using Lenti-X concentrator (Clontech) and resuspended in PBS. Virus was stored at -80°C. DRG neurons were infected after 1 day *in vitro*. Infection efficiency as assessed by Venus fluorescence was similar across SARM1 variants.

**Culture of Dorsal Root Ganglion Neurons**. Primary DRG cells were isolated from embryonic day 13.5 $SARM^{-/-}$ embryos as previously described (12). They were seeded on plates coated with poly-D-lysine and laminin. Neurons were maintained in neurobasal medium supplemented with L-glutamine (Invitrogen), 2% B27 (Invitrogen), 50ng/ml nerve growth factor (Harlan Laboratories), 1 μM 5-fluoro-2'-deoxyuridine (Sigma), and 1 μM uridine (Sigma) to induce death of mitotic cells. Cultures were transduced with lentivirus after 1 day *in vitro*.

**Metabolite Extraction from DRG Neurons**. After 6 days *in vitro*, plates were placed on ice and culture medium was replaced with ice-cold saline (0.9% NaCl in water, 500μl per well). For collection of intracellular metabolites, saline was removed and replaced with 160 μL ice-cold 50% MeOH in water. Plates were incubated for 5 min on ice and then metabolite-containing solutions were transferred to tubes containing 50 μl chloroform on ice, taking care not to disturb cells. Tubes were shaken vigorously, and then centrifuged at 20,000 g for 15 min at 4°C. The clear aqueous phase (140 μl) was transferred into a new tube and lyophilized. Lyophilized samples were stored at -20°C until measurement.

**Metabolite Measurement by LC-MS/MS**. Lyophilized samples were reconstituted with 5 mM ammonium formate (15 μl), centrifuged (20,000 g, 10 min, 4°C), and 10 μl of clear supernatant was analyzed using LC-MS (13, 14). Samples were injected into C18 reverse phase column (Atlantis T3, 2.1 x 150 mm, 3 μm; Waters) equipped with HPLC system (Agilent 1290 LC) at a flow rate of 0.15 ml/min with 5 mM ammonium formate for mobile phase A and 100% methanol for mobile phase B. Metabolites were eluted with gradients of 0–10 min, 0–70% B; 10–15 min, 70% B; 16–20 min, 0% B. The metabolites were detected with a triple quad mass spectrometer (Agilent 6470 MassHunter; Agilent) under positive ESI multiple reaction monitoring (MRM) using parameters for $NAD^+$ (precursor m/z = 664, product m/z = 428, fragmentation (F) = 160 V, collision (C) = 22 V, and cell acceleration (CA) = 7 V). Serial dilutions of $NAD^+$ in 5 mM ammonium formate were used to generate the standard curve. Metabolites were quantified by MassHunter quantitative analysis tool (Agilent) and normalized by the protein amount.

**Measurement of Axon Fragmentation**. DRGs were seeded into 96-well plates and distal axons were imaged using a high-content Operetta imager (PerkinElmer) 5 days post infection. A previously designed ImageJ macro (12) was used to quantify axon degeneration from bright-field images by calculating a ratio of fragmented axon area to total axon area. For each experiment, this axon degeneration index was averaged over nine fields per well and four wells per condition.

**Sensitized Emission FRET**. Measurements of FRET intensity of SARM1-FRET constructs were performed as previously described (15). HEK293T cells were transfected with SARM1-FRET constructs and imaged using the Operetta imager 48 h later. Intensity of the C-terminal mCerulean donor fluorophore was measured with a 430/25 excitation filter and 470/30 emission filter. FRET images were collected with a 430/25 excitation filter and 525/20 emission filter. Corrected FRET intensity was calculated by subtracting the amount of donor signal bleed through from the raw FRET intensity. The relative FRET intensity measurement was then calculated as the corrected FRET intensity divided by the donor intensity.

**Statistical Analyses**. At least three independent biological replicates were completed for each experiment and error bars represent SEM. Statistical tests of one- or two-way ANOVA were performed where appropriate to compare experimental conditions to a given control. To denote statistical significance, *$p<0.05$, **$p<0.01$, and ***$p<0.001$. Tests were performed using Graph Pad Prism 5.

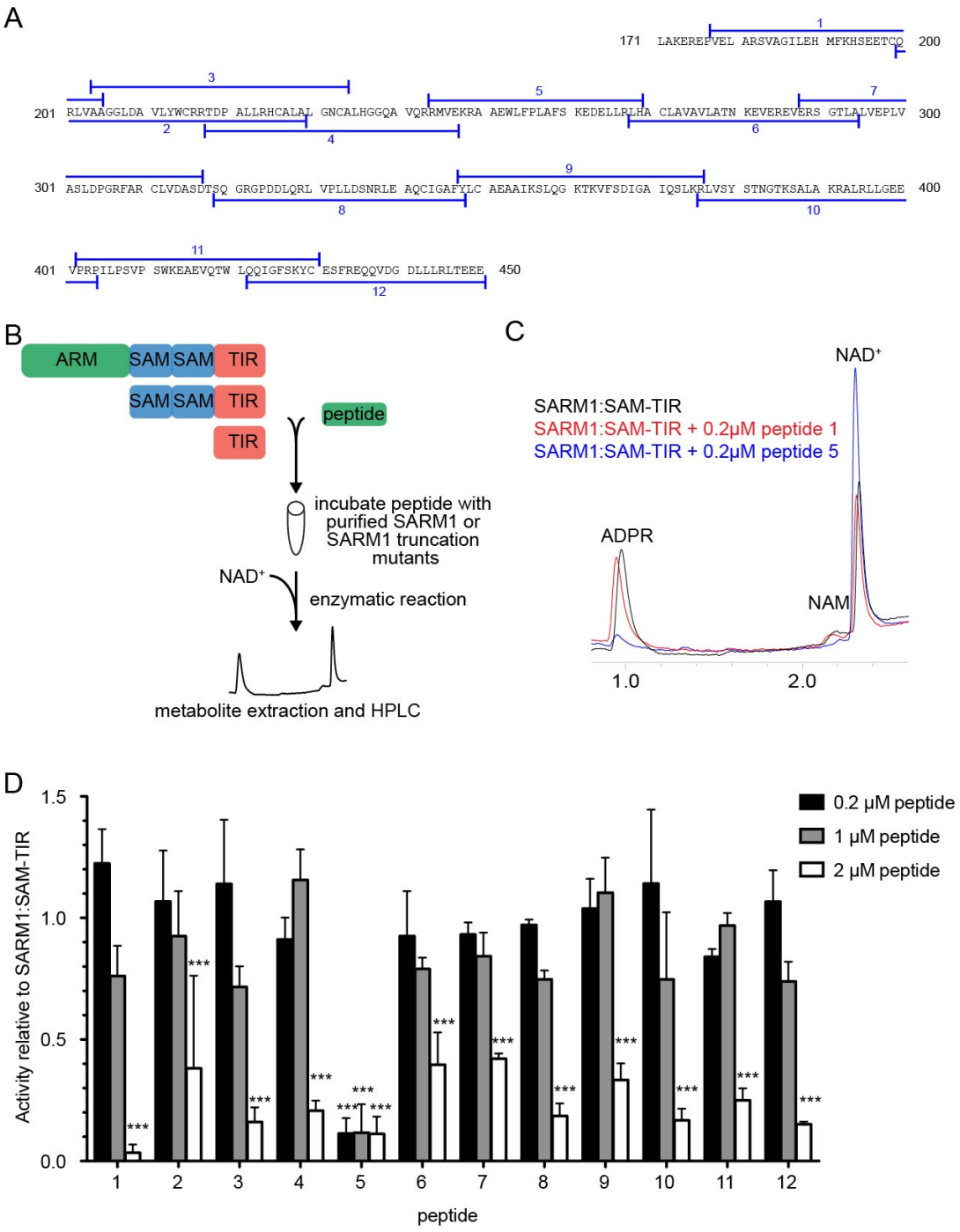


**Figure S1.** A peptide derived from the N-terminus can inhibit SARM1 NADase activity *in vitro*. (A) Schematic of the most evolutionarily conserved portion of the SARM1 N-terminus from V183 to E450 and the 12 short peptides designed to tile this region. (B) Schematic of the *in vitro* NADase assay. (C) HPLC chromatogram of $NAD^+$ hydrolysis by purified SARM1:SAM-TIR in the presence of peptide 1 or peptide 5. Positions designating $NAD^+$, nicotinamide (Nam), and ADPR peaks were determined by known standards. (D) Ability of each peptide to block SARM1:SAM-TIR NADase activity, calculated as amount of ADPR detected by HPLC relative to SARM1:SAM-TIR without peptide. Error bars represent SEM, n = 3, two-way ANOVA with Bonferroni post-test was used for statistical analysis with ***p<0.001.

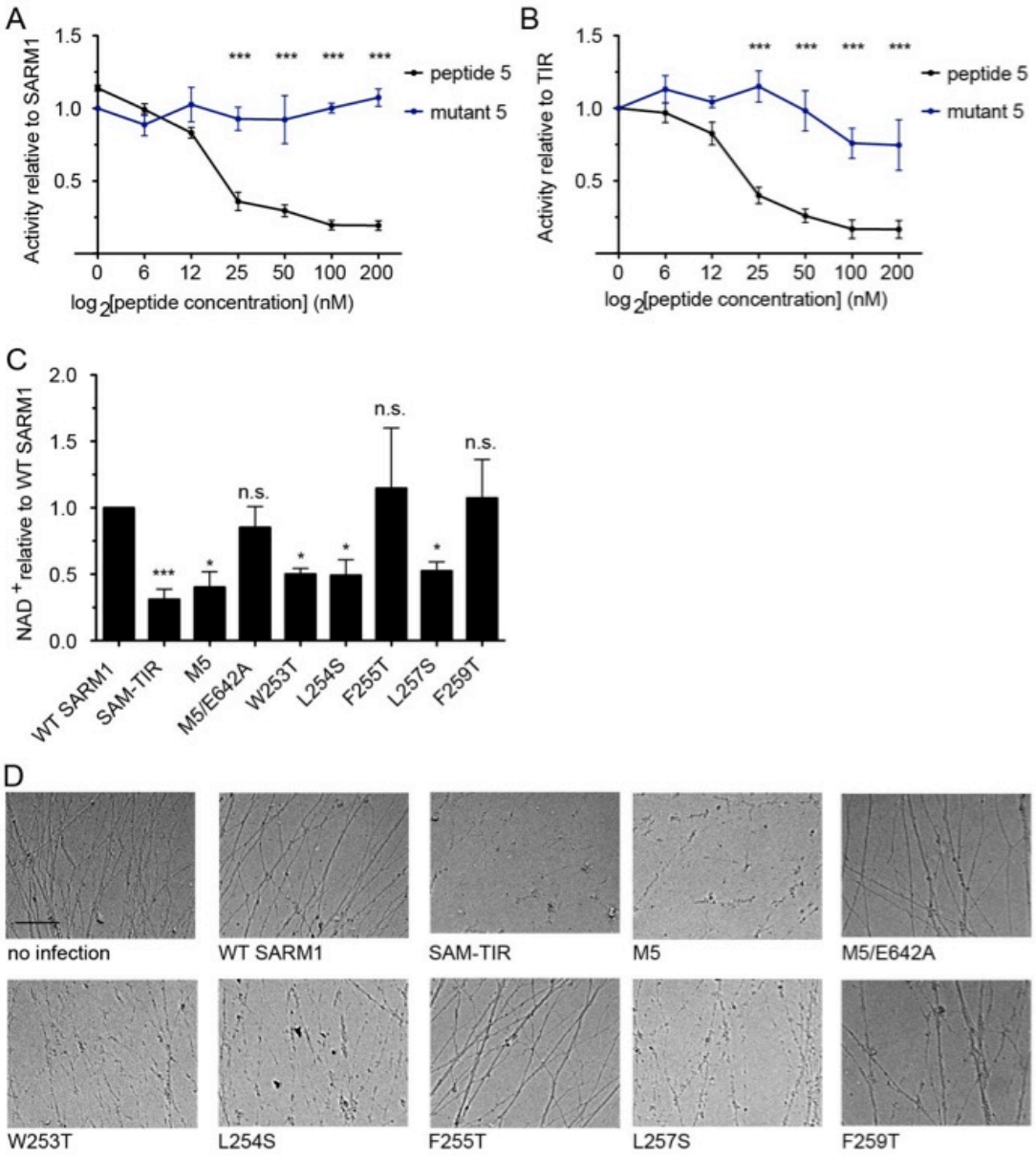


**Figure S2.** A conserved hydrophobic region of peptide 5 mediates inhibition of SARM1 NADase and prodegenerative activity. (A) Two-fold dose response curves for peptide-mediated inhibition of full-length SARM1 NADase activity *in vitro*. Error bars represent +/- SEM. N = 4-6, two-way ANOVA was used for statistical analysis with ***p<0.001. (B) Two-fold dose response curves for peptide-mediated inhibition of TIR NADase activity *in vitro*. Error bars represent +/- SEM. N = 4-6, two-way ANOVA was used for statistical analysis with ***p<0.001. (C) DRG sensory neurons from SARM1 KO mice were infected with variants of SARM1 and metabolites were extracted 3d post infection to measure $NAD^+$ levels relative to neurons infected with wild-type SARM1. Error bars represent SEM, n = 4, one-way ANOVA with Dunnett post-test was used for statistical analysis with *p<0.05, ***p<0.001. (D) DRG sensory neurons from SARM1 KO mice were infected with variants of SARM1 and axons were imaged 5d later (scale bar, 50μM).

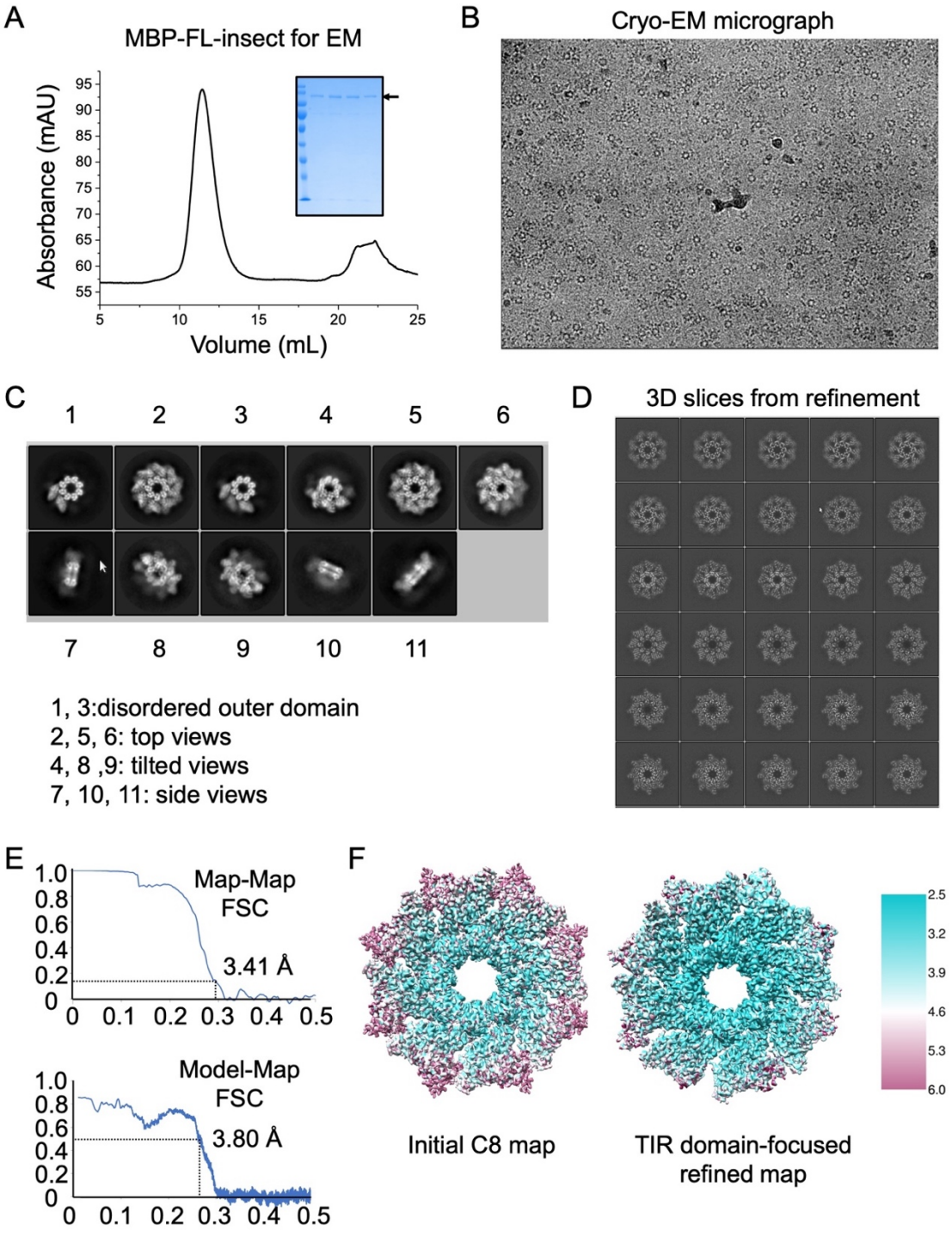


**Figure S3.** Purification and structure determination of human SARM1. (A) Gel-filtration profile of MBP-SARM1 over a Superdex 200 column. (B) A represented cryo-EM micrograph. (C) Representative 2D class averages. (D) 3D slices of the reconstructed map with C8 symmetry applied. (E) Gold standard map-map FSC and model-map FSC as indications of the resolution. (F) Local resolution of the final C8-averaged map, and TIR domain-focused refined map.

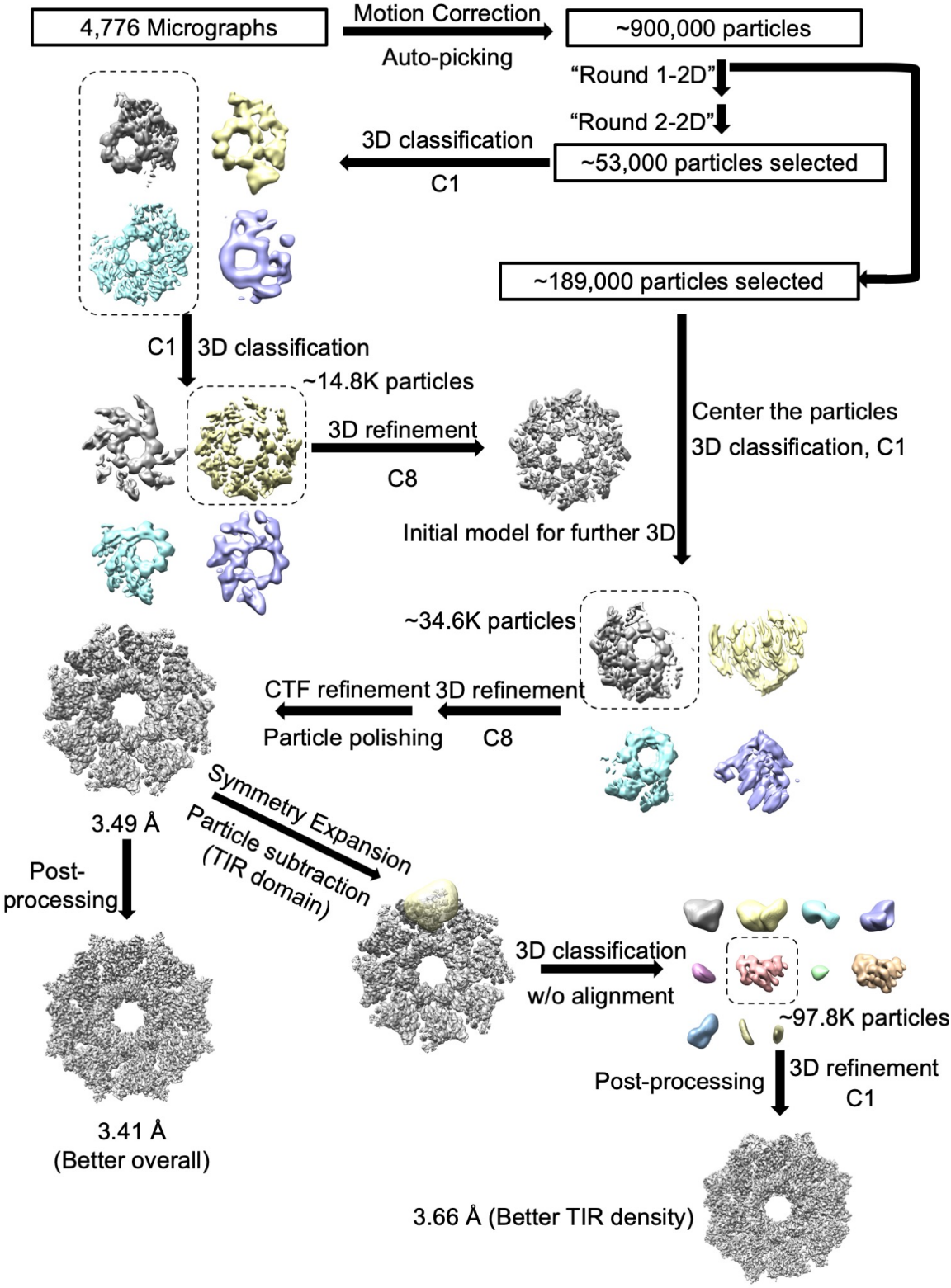


**Figure S4**. Flow chart of cryo-EM data processing.

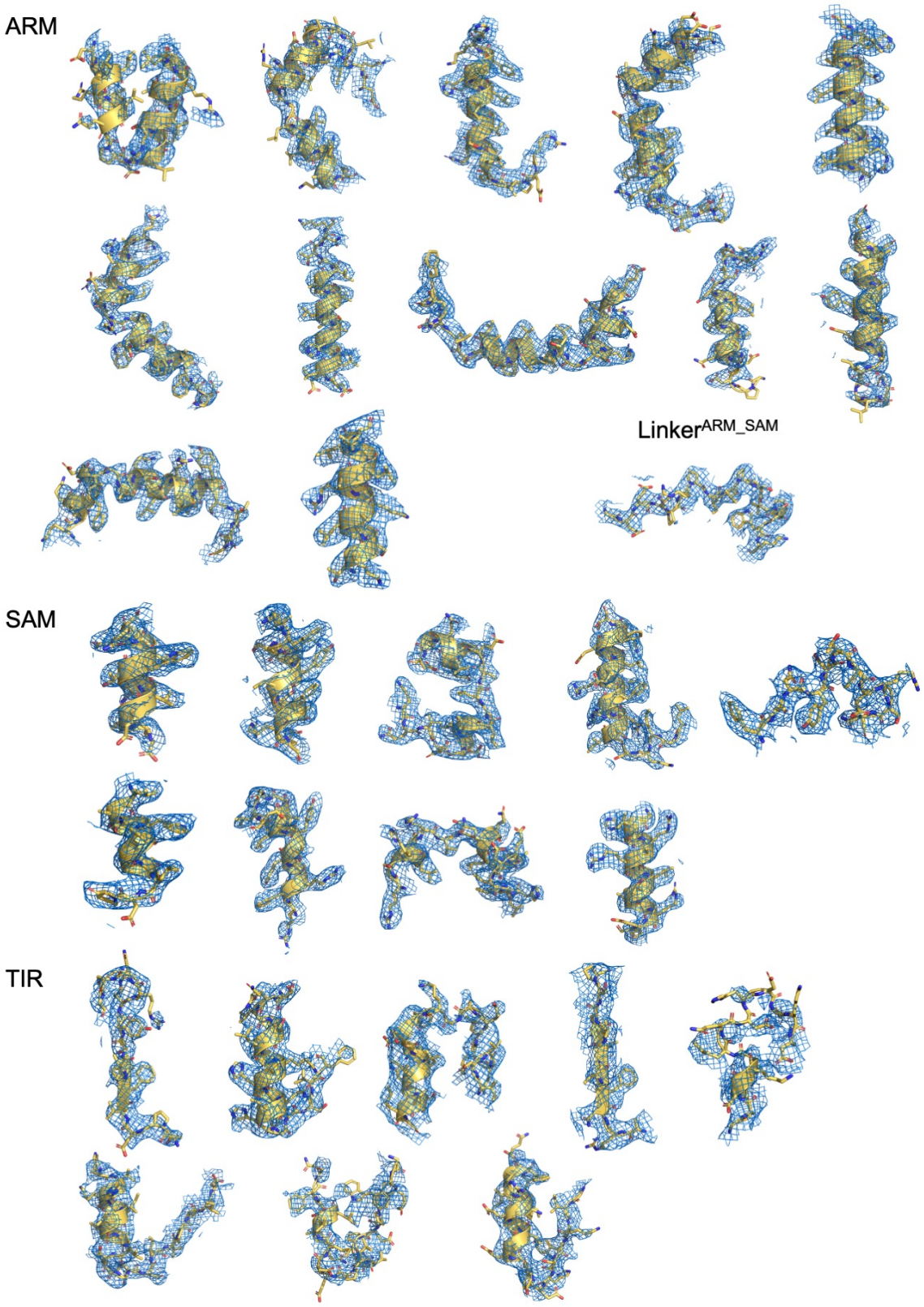


**Figure S5**. Segments from different domains fitted with the cryo-EM density map.

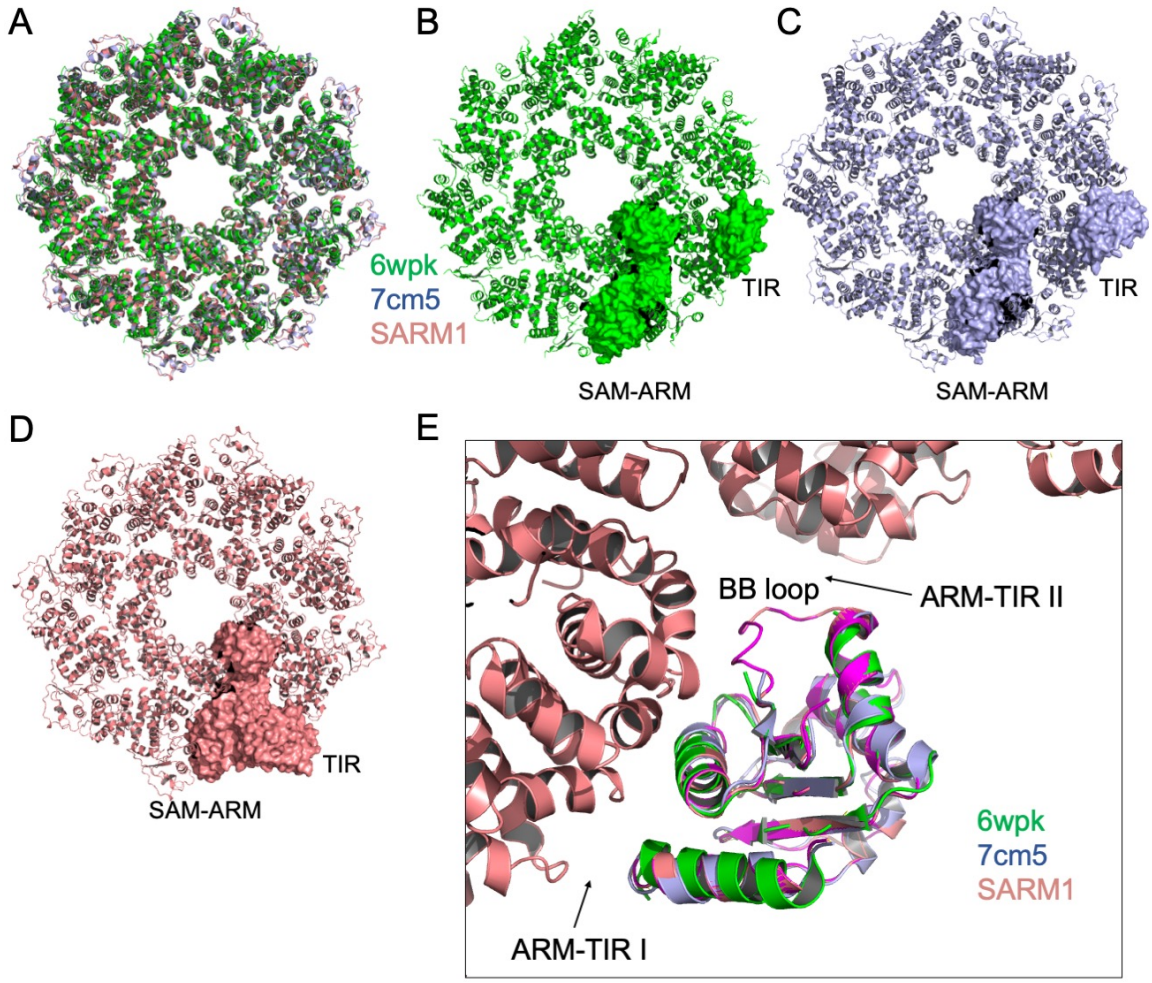


**Figure S6**. Comparison with published SARM1 octamer structures (16, 17), highlighting the difference in the TIR domain. (A) Ribbon diagram of our structure aligned with the published structures, showing the overall similarity. (B, C) Ribbon diagrams of the published structures with one protomer shown. (D) A different assignment of the protomer in which the TIR domain is in direct contact with the SAM-ARM domains intramolecularly. (E) Superimposed TIR domains from our structure and the two published structures shown adjacent to the intramolecular and intermolecular ARM domains. The BB loop important for TIR catalysis is only visible in our structure.


**Figure S7**. Cryo-EM structure-based secondary structure annotation on full-length SARM1.

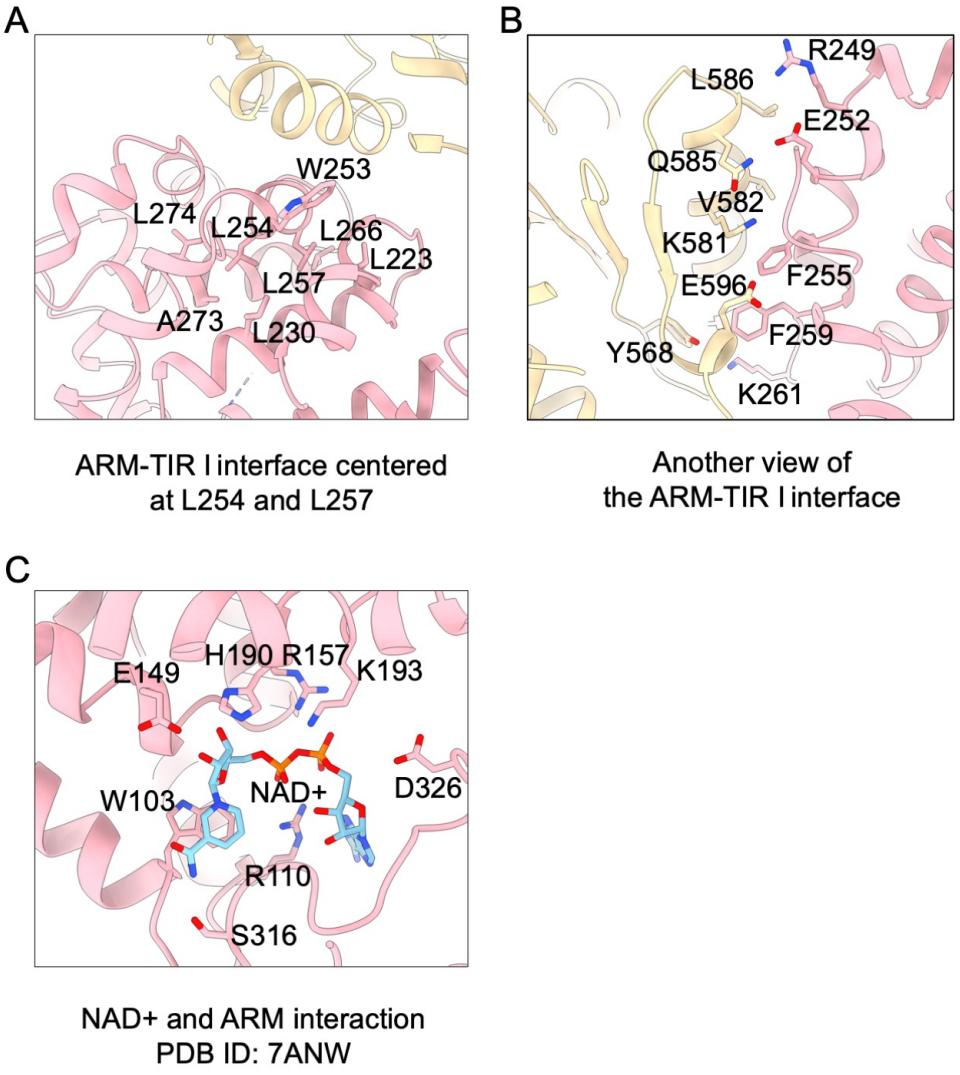


**Figure S8**. Other views of the ARM-TIR I interface. (A) A view centered at L254 and L257, which are buried in a hydrophobic pocket within the ARM domain itself. (B) Another view of the ARM-TIR I interface to emphasize residues F255 and F259. (C) Detailed interaction between $NAD^+$ and ARM domain from $NAD^+$-bound SARM1 structure (PDB ID: 7ANW).

**Table S1.** Statistics of SARM1 Cryo-EM Structure

| EM data collection | |
|---|---|
| Voltage (keV) | 300 |
| Defocus range (μm) | 1.2 - 2.5 |
| Number of images | 4776 |
| Number of particles(final) | 34643 |

| Model | |
|---|---|
| Resolution (Å) | 3.8 |
| Number of protein residues | 4704 |
| Number of atoms | 37136 |
| Ramachandran statistics | |
| Favored regions (%) | 88.64 |
| Allowed regions (%) | 11.36 |
| Disallowed regions (%) | 0.0 |
| Rotamer outliers (%) | 1.04 |
| Clash score | 19.0 |

## References


1. K. Essuman, *et al.*, The SARM1 Toll / Interleukin-1 Receptor Domain Possesses Intrinsic NAD + Cleavage Activity that Promotes Pathological Axonal Degeneration. *Neuron* **93**, 1334-1343.e5 (2017).
2. S. Q. Zheng, *et al.*, MotionCor2: Anisotropic correction of beam-induced motion for improved cryo-electron microscopy. *Nat. Methods* **14**, 331–332 (2017).
3. A. Rohou, N. Grigorieff, CTFFIND4: Fast and accurate defocus estimation from electron micrographs. *J. Struct. Biol.* **192**, 216–221 (2015).
4. T. Wagner, *et al.*, SPHIRE-crYOLO is a fast and accurate fully automated particle picker for cryo-EM. *Commun. Biol.* **2**, 1–13 (2019).
5. S. H. W. Scheres, RELION: Implementation of a Bayesian approach to cryo-EM structure determination. *J. Struct. Biol.* **180**, 519–530 (2012).
6. A. Kucukelbir, F. J. Sigworth, H. D. Tagare, Quantifying the local resolution of cryo-EM density maps. *Nat. Methods* **11**, 63–65 (2014).
7. M. Biasini, *et al.*, SWISS-MODEL: Modelling protein tertiary and quaternary structure using evolutionary information. *Nucleic Acids Res.* **42**, 252–258 (2014).
8. S. Horsefield, *et al.*, NAD+ cleavage activity by animal and plant TIR domains in cell death pathways. *Science* **365**, 793–799 (2019).
9. P. Emsley, K. Cowtan, Coot: Model-building tools for molecular graphics. *Acta Crystallogr. Sect. D Biol. Crystallogr.* **60**, 2126–2132 (2004).
10. P. D. Adams, *et al.*, PHENIX: A comprehensive Python-based system for macromolecular structure solution. *Acta Crystallogr. Sect. D Biol. Crystallogr.* **66**, 213–221 (2010).
11. W. L. Delano, The PyMOL Molecular Graphics System (2002).
12. Y. Sasaki, B. P. S. Vohra, F. E. Lund, J. Milbrandt, Nicotinamide Mononucleotide Adenylyl Transferase-Mediated Axonal Protection Requires Enzymatic Activity But Not Increased Levels of Neuronal Nicotinamide Adenine Dinucleotide. *J. Neurosci.* **29**, 5525–5535 (2009).
13. K. Hikosaka, *et al.*, Deficiency of nicotinamide mononucleotide adenylyltransferase 3 (Nmnat3) causes hemolytic anemia by altering the glycolytic flow in mature erythrocytes. *J. Biol. Chem.* **289**, 14796–14811 (2014).
14. Y. Sasaki, T. Nakagawa, X. Mao, A. DiAntonio, J. Milbrandt, NMNAT1 inhibits axon degeneration via blockade of SARM1-mediated NAD+depletion. *Elife* **5**, 1–15 (2016).
15. D. W. Summers, D. A. Gibson, A. DiAntonio, J. Milbrandt, SARM1-specific motifs in the TIR domain enable NAD $^{+}$ loss and regulate injury-induced SARM1 activation. *Proc. Natl. Acad. Sci.* **113**, E6271–E6280 (2016).
16. Y. Jiang, *et al.*, The NAD+-mediated self-inhibition mechanism of pro-neurodegenerative Sarm1. *Nature* (2020) https:/doi.org/10.1038/s41586-020-2862-z.
17. M. Bratkowski, *et al.*, Structural and Mechanistic Regulation of the Pro degenerative NAD Hydrolase SARM1. *Cell Rep.* **32**, 107999 (2020).